



This is a repository copy of *Thermal treatment of nuclear fuel-containing Magnox sludge radioactive waste*.

White Rose Research Online URL for this paper:
<https://eprints.whiterose.ac.uk/173014/>

Version: Accepted Version

Article:

Barlow, S.T., Fisher, A.J., Bailey, D.J. orcid.org/0000-0002-0313-8748 et al. (6 more authors) (2021) Thermal treatment of nuclear fuel-containing Magnox sludge radioactive waste. *Journal of Nuclear Materials*, 552. 152965. ISSN 0022-3115

<https://doi.org/10.1016/j.jnucmat.2021.152965>

© 2021 Elsevier. This is an author produced version of a paper subsequently published in *Journal of Nuclear Materials*. Uploaded in accordance with the publisher's self-archiving policy. Article available under the terms of the CC-BY-NC-ND licence (<https://creativecommons.org/licenses/by-nc-nd/4.0/>).

Reuse

This article is distributed under the terms of the Creative Commons Attribution-NonCommercial-NoDerivs (CC BY-NC-ND) licence. This licence only allows you to download this work and share it with others as long as you credit the authors, but you can't change the article in any way or use it commercially. More information and the full terms of the licence here: <https://creativecommons.org/licenses/>

Takedown

If you consider content in White Rose Research Online to be in breach of UK law, please notify us by emailing eprints@whiterose.ac.uk including the URL of the record and the reason for the withdrawal request.



eprints@whiterose.ac.uk
<https://eprints.whiterose.ac.uk/>

1 Thermal treatment of nuclear fuel-containing
2 Magnox sludge radioactive waste

3

4 Sean T. Barlow¹, Adam J. Fisher¹, Daniel J. Bailey¹, Lewis R. Blackburn¹, Martin C. Stennett¹, Russell J.
5 Hand¹, Sean P. Morgan², Neil C. Hyatt¹ and Claire L. Corkhill^{1*}

6

7 ¹NucleUS Immobilisation Science Laboratory, Department of Materials Science & Engineering, The
8 University of Sheffield, Sheffield S1 3JD, UK

9 ²Sellafield Ltd., Hinton House, Risley, Warrington WA3 6GR, UK

10

11 *Corresponding author: c.corkhill@sheffield.ac.uk

12

13

14

15

16

17

18

19

20

21

22

23

24

25

26

27

28

29 **Abstract**

30 Magnesium aluminosilicate and magnesium borosilicate glass formulations were developed and
31 evaluated for the immobilisation of the radioactive waste known as Magnox sludge. Glass compositions
32 were synthesised using two simplified bounding waste simulants, including corroded and metallic
33 uranium and magnesium at waste loadings of up to 50 wt.%. The glasses immobilising corroded
34 simulant waste formed heterogeneous and fully amorphous glasses, while those immobilising metallic
35 wastes contained crystallites of UO_2 and U_3O_8 . Uranium speciation within the glass was investigated by
36 micro-focus X-ray absorption near edge spectroscopy and it was shown that the borosilicate glass
37 compositions were characterised by a slightly lower mean uranium oxidation state than the
38 aluminosilicate counterparts. This had an impact upon the durability, and uranium within glasses of
39 higher mean oxidation states was dissolved more readily. All material showed dissolution rates that
40 were comparable to simulant high level radioactive waste glasses, while the borosilicate-based
41 formulations melted at a temperature suitable for modern vitrification technologies used in radioactive
42 waste applications. These data highlights the potential for vitrification of hazardous radioactive Magnox
43 sludge waste in borosilicate or aluminosilicate glass formulations, with the potential to achieve >95 %
44 reduction in conditioned waste volume over the current baseline plan.

45

46 **Key words:** radioactive waste, Magnox sludge, glass, thermal treatment.

47

48

49

50

51

52

53

54

55

56

57

58

59

60 1. Introduction

61

62 The United Kingdom operated Magnox nuclear reactors for electricity production from 1953 to 2015.
63 These first generation graphite-moderated, carbon dioxide-cooled reactors used natural, unenriched
64 uranium metal fuel clad in a *magnesium non-oxidising* (Magnox) alloy. Although all Magnox reactors
65 are now in the process of being decommissioned, wastes arising from Magnox spent fuel management
66 continue to pose a radiological risk. Historically, Magnox spent nuclear fuel was stored at Sellafield, UK,
67 in open air water-filled cooling ponds (the First Generation Magnox Storage Ponds, FGMSF) prior to
68 reprocessing [1] and the sheared cladding was also stored underwater in the Magnox Swarf Storage
69 Silos (MSSS). Increased throughput of nuclear fuel during the 1970s and 1980s at Magnox stations,
70 combined with lengthy shutdowns at the reprocessing facility, led to a build-up of spent nuclear fuel in
71 the FGMSF and MSSS resulting in storage periods longer than originally anticipated. Increased storage
72 times led to considerable corrosion of the Magnox alloy fuel cladding by water according to Eqn 1., in
73 addition to corrosion of metallic uranium fuel, forming radiologically hazardous magnesium hydroxide
74 sludge, incorporating partially, or fully corroded spent nuclear fuel, on the bottom of the cooling pond:

75



77

78 The baseline treatment strategy for this material, known as Magnox sludge [1], is retrieval from the
79 ponds, silos and other locations (e.g. bulk storage tanks containing effluent from the Site Ion Exchange
80 Effluent Plant, SIXEP) and storage in an engineered facility prior to encapsulation in a cement matrix,
81 consistent with the conditioning of other intermediate level wastes. Although cost effective in the
82 short-term, cementation increases the volume of waste requiring disposal, thereby increasing the
83 storage, transport and overall cost of a geological disposal facility, the UK's preferred disposal option
84 for higher activity radioactive waste. Furthermore, water entrained within cement pore water may
85 promote corrosion of metallic cladding or fuel fragments within the sludge, leading to volume
86 expansion [2,3] and generation of hydrogen gas disposal [4 – 6]; therefore, a cemented wastefrom is
87 unlikely to remain passive over the time scales required for storage.

88

89 In contrast, thermal treatment of radioactive wastes is widely accepted to produce passively safe
90 wastefroms, and vitrification is utilised for the immobilisation of spent fuel reprocessing wastes in a
91 mixed alkali (Li/Na) borosilicate glass. A range of technologies are currently being explored for the
92 thermal treatment (vitrification) of a wide range of radioactively contaminated decommissioning
93 wastes in the UK [3, 7-10], and elsewhere, based on alkali/alkaline-earth modified silica-glass materials.

94 Aluminosilicate glass compositions have been considered previously for immobilisation of high activity
95 wastes, most notably Hanford tank wastes [11]. The final products of such vitrification, depending on
96 the technology applied, are expected to be highly variable in composition and heterogeneity, forming
97 fully vitreous products or glass-ceramic materials. Indeed, we recently reported characterisation of
98 such heterogeneous wasteforms produced at demonstration scale by in container vitrification of
99 simulant UK ILW wastes [10]. The chemical and physical heterogeneity of these wasteforms arises from
100 local chemical gradients, due to feed heterogeneity, and realistic melt convection which is nevertheless
101 insufficient to fully homogenise the melt during the process time. Our experiments are constructed to
102 approximate this process, albeit at smaller scale, and are thus considered a reasonable approximation
103 to the heterogeneous products that would be afforded by e.g. by in container vitrification technology.
104 It should be noted that it is not the intention that such thermally treated wasteforms should be formed
105 as homogeneous products, as for example, is the case with vitrified HLW [e.g. 12- 14]. Rather, it is the
106 intention that the wasteform is produced as a passively safe material that meets disposability
107 requirements, because the variability of the ILW feed between batches means that homogeneous
108 products cannot be guaranteed.

109

110 In this study, we describe an investigation to develop Mg-based alumino- and boro-silicate glass
111 compositions suitable for the immobilisation of Magnox sludge, by conventional or in-container Joule
112 heated melter technology, incorporating a wide waste envelope, from fully corroded Mg and U oxides,
113 to metallic Mg and U.

114

115 **2. Materials and methods**

116

117 *2.1 Synthesis and characterisation*

118 Two potentially suitable base glass compositions were developed through a study of the low
119 temperature isotherms of magnesium borosilicate (MBS) and magnesium aluminosilicate (MAS)
120 pseudo-ternary liquidus phase diagrams [15, 16]. Since the composition of Magnox sludge is highly
121 variable [1, 17], two simplified bounding extremes of the Magnox sludge waste were investigated, as
122 detailed in Table 1, including: (i) *metallic waste*, consisting of mostly intact uranium metal fuel and
123 metallic Magnox cladding material and; (ii) *corroded waste* - containing highly corroded Magnox
124 cladding with uranium oxide contamination. In our study depleted uranium was used as an analogue
125 for spent Magnox fuel and boron was also added in a trace quantity to the MAS compositions as a tracer
126 for evaluation of the chemical durability of the glassy wasteform [18]. A combination of the base glass
127 systems and the bounding extreme wastes resulted in the fabrication of a suite of six samples including

128 two base glasses (MBS and MAS), two glasses containing the “corroded” waste fraction, designated as
129 MBS-C and MAS-C, and two glassy materials containing the “metallic” waste fraction, MBS-M and MAS-
130 M.

131

132 Glasses were fabricated from stoichiometric quantities of SiO₂, H₃BO₃ (Sigma-Aldrich 99.5%), Na₂CO₃
133 (Alfa Aesar 98%), Al(OH)₃ (Acros 95%), Mg(OH)₂ (Sigma-Aldrich 95%), Mg (Acros 99.9%), U₃O₈ and U
134 (British Nuclear Fuels Ltd.), and were batched and mixed together by hand for 3 minutes before melting
135 in alumina crucibles within an Elite Thermal Systems BRF15/5 muffle furnace. The Mg content in the
136 base glass samples was replaced, on a molar basis, with the proportion of Mg found in the bounding
137 waste compositions (Table 1) and renormalized to create the waste loaded formulations including U.
138 Hence, the total waste loading (mol. %) is considered as the total Mg and U contribution expressed as
139 oxides (Table 2). MBS compositions were melted at 1250 °C for 3 hours (annealed at 610 °C for 1 hour)
140 and MAS compositions were melted at 1500 °C for 5 hours (annealed at 560 °C for one hour) to form
141 fluid melts. The melts were not stirred, to promote the heterogeneity expected in the full scale process.
142 All glasses were cast as ingots on heated steel plates, as shown in Figure 1; note the yellow-brown
143 colour of the MAS-corroded glass, in thin section, characteristic of incorporated U(VI). Glass
144 compositions were determined via total dissolution in hydrofluoric acid and analysed by Inductively
145 Coupled Plasma Optical Emission Spectroscopy (ICP-OES), as shown in Table 2.

146

147 **Table 1.**

148 Bounding waste compositions for First Generation Magnox Storage Ponds

	Mg	Mg(OH) ₂	U	U ₃ O ₈
Metallic waste (wt. %)	12.0	20.0	68.0	0.0
Corroded waste (wt. %)	5.0	80.0	5.0	10.0

149

150

151

152

153

154

155

156

157

158

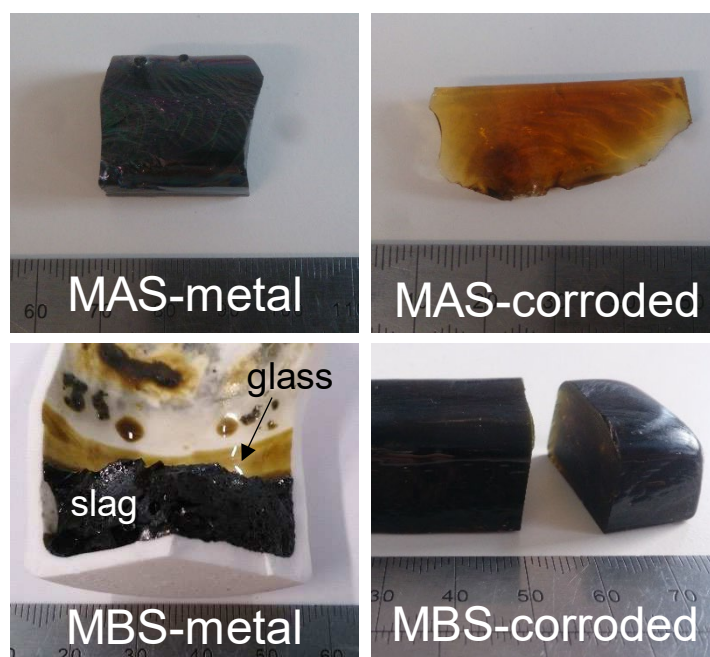
159 **Table 2.**

160 Analysed glass compositions (mol. %) as determined by ICP-OES analysis of digested samples.

	MAS	MAS-M	MAS-C	MBS	MBS-M	MBS-C
<i>Analysed composition (± 0.2) mol. %</i>						
SiO ₂	46.4	42.8	44.7	24.4	23.2	24.5
B ₂ O ₃	1.8	3.3	1.3	24.1	21.7	23.1
MgO	20.5	23.7	27.6	47.6	41.7	47.4
UO ₃	-	4.1	0.5	-	6.9	0.7
Na ₂ O	20.6	15.6	18.8	-	-	-
Al ₂ O ₃	10.7	10.5	7.1	3.9	6.5	4.3
<i>Wasteloading (MgO + UO₃)</i>	-	27.8	28.1	-	48.6	48.1
<i>Density (g cm⁻³)</i>	2.58 \pm 0.01	3.24 \pm 0.01	2.68 \pm 0.01	2.63 \pm 0.01	3.72 \pm 0.01	2.76 \pm 0.01

161

162



163 **Fig. 1.** Photographs of the glass compositions. For MBS-metal, the slag fraction that remained at the bottom of
164 the crucible, after the glass fraction was poured (with glassy remnants adhered to the crucible), is highlighted.

165

166 During glass melting, no violent or unduly vigorous reactions between the waste simulants, including
167 the metallic content, and glass were observed; however, corrosion of the alumina crucibles did occur,
168 which increased the Al₂O₃ content by several mol. % compared to the targeted amount. The MBS-M

169 composition was viscous and although a glass was poured, a glassy slag-like fraction remained at the
170 bottom of the crucible (see Figure 1). The desired UO_3 content of this glass was 14.5 mol. %, however,
171 only around half of this was retained in the glass (Table 2), indicating that the slag fraction retained a
172 significant proportion of the uranium metal added. It should be noted that these melts were not stirred,
173 which may have facilitated settling of heavy U-metal at the bottom of the crucible. Such segregation,
174 into a glass and metal-rich slag, has commonly been observed when metal-containing waste streams
175 are subject to in-can vitrification trials of radioactive waste surrogates [e.g. 3, 7, 9, 10], therefore it was
176 decided not to re-melt the glass with stirring, but to proceed with analysis of the segregated glass, as a
177 conservative scenario.

178
179 Glass powders (pre- and post-dissolution, < 75 μm and 75 - 150 μm diameter, respectively) were
180 characterised by powder X-ray diffraction (XRD) using a Bruker D2 X-ray diffractometer in reflection
181 mode over the range $10^\circ < 2\theta < 60^\circ$ using $\text{Cu K}\alpha$ radiation (30 kV, 10 mA); $\text{K}\beta$ radiation was stripped
182 using a Ni foil filter. XRD data were processed using the Bruker DiffractionEva 3.0 software package with
183 Crystallography Open Database and the International Centre for Diffraction Data (ICDD) database. The
184 densities of glass samples were determined by helium pycnometry using a Micromeritics Accupyc II
185 1340 with < 75 μm powder samples; errors reported are the standard deviation of triplicate
186 measurements (Table 2).

187
188 The microstructure of the glass samples and distribution of elements contained within, in cross-section,
189 was characterised by Scanning Electron Microscopy and Energy Dispersive X-ray spectroscopy (SEM-
190 EDX) using a Hitachi TM3030-SEM equipped with a Bruker Quantax EDX system. Sectioned glass
191 samples and recovered glass powder from dissolution experiments were prepared for SEM analysis by
192 mounting in cold-setting resin and polishing to an optical finish (1 μm) using progressively finer grades
193 of SiC papers and diamond suspension. Recovered glass powders from 28 d PCT-B tests (see below)
194 were also observed in whole by attachment to carbon tabs to probe potential alteration features.

195
196 X-ray Absorption Near-Edge Spectroscopy (XANES) was performed in micro-focus mode to determine
197 the oxidation state of uranium in the glass [19 – 21]. Samples were measured in fluorescence mode at
198 the X05LA beamline, Paul Scherrer Institute Swiss Light Source (Switzerland), at the U L_3 edge
199 (17166 eV). Measurements were made on a motorised 3D stage allowing scanning of samples with a
200 beam spot size of approximately 1 μm^2 and photon energy tuned using a double crystal Si (111)
201 monochromator. Multiple XANES spectra for each sample were measured and averaged at the regions
202 of interest over the range $30 \text{ eV} \leq \text{U } L_3 \text{ edge} \leq 250 \text{ eV}$. X-ray fluorescence (XRF) was measured using a

203 Si drift detector (KETEK) mounted 45° to the incident beam, creating XRF maps to aid selecting regions
204 of interest. Data reduction and XANES analysis were performed using the Athena Demeter 0.9.24
205 software package [22]. Uranium oxidation state was determined by linear regression with respect to
206 standards of known oxidation state: UTi_2O_6 (U^{4+}), $U_{0.5}Y_{0.5}Ti_2O_6$ (U^{5+}) and $CaUO_4$ (U^{6+}) [23, 24]. The
207 utilisation of a micro-focused beam allowed selection of areas where there were no apparent crystalline
208 phases. We attempted to acquire U L_3 micro-focus XANES data from the U-poor glass phase apparent
209 in the microstructure of the MBS-C glass, as observed by SEM-EDX, however the concentration was too
210 low to permit acquisition of data with acceptable signal to noise ratio.

211

212 *2.2 Chemical durability analysis*

213 The chemical durability of the glass compositions was assessed using a modified ASTM Product
214 Consistency Test B (PCT-B) protocol [25]. Powdered samples with a 75 - 150 μm diameter size fraction
215 were dissolved in Ultra-High Quality (UHQ) water (18.2 M Ω cm) at 90 °C for 28 days with a surface area
216 to volume ratio of 1,200 m^{-1} . The surface area was determined geometrically according to the PCT-B
217 protocol. Solution was sampled from duplicate sacrificial vessels after 1, 3, 7, 14, 21 and 28 days.
218 Elemental concentration in solution was determined by ICP-OES using a Thermo-Fisher iCAP 6300Duo
219 instrument.

220

221 The durability was expressed as the normalised mass of element (i) in $g\ m^{-2}$ (NL_i), according to:

222

$$223 \quad NL_i = (C_i - C_{i,b}) / (f_i \times (SA/V)) \quad (2)$$

224

225 where C_i and $C_{i,b}$ are the average concentration of element, i , in the leachate and blank tests (solution
226 only, no glass), respectively ($mg\ L^{-1}$), f_i is the mass fraction of i in the glass (unitless) and SA/V is the
227 surface area to volume ratio of the total particles (m^{-1}), based on the geometric surface area.
228 Uncertainty in NL_i was calculated by the standard deviation of the sum of uncorrelated random errors.
229 Geochemical modelling of the leachate chemistry was performed by PHREEQ-C to calculate the
230 saturation indices of various secondary phases in the leachates after 28 days. The concentration of
231 elements in the leachate and the leachate pH(RT) were used as input to calculate a range of secondary
232 phases saturated in solution according to the Lawrence Livermore National Laboratory (LLNL) database.

233

234

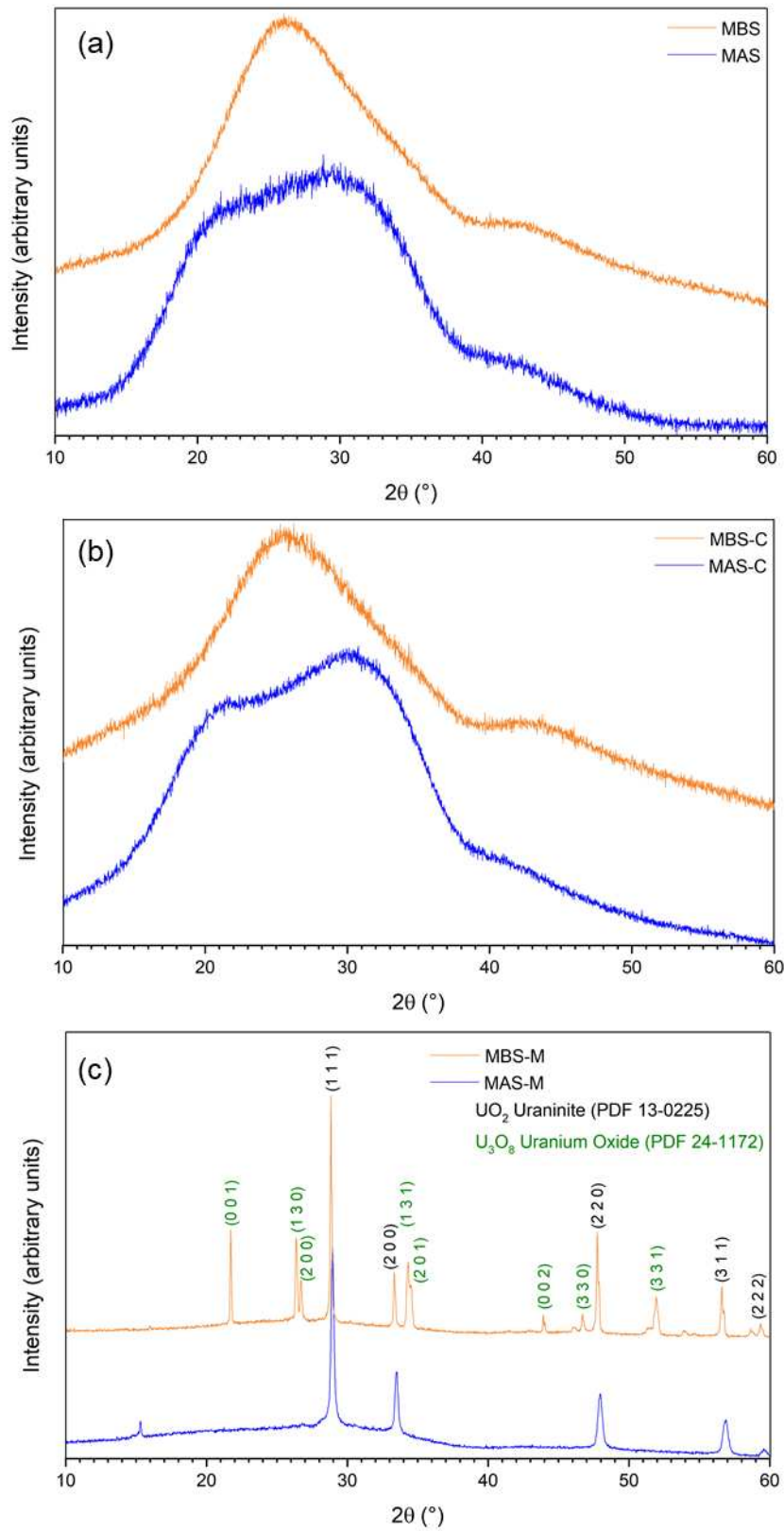
235 3. Results and Discussion

236

237 *3.1 Phase analysis and microstructure*

238 X-ray diffraction analysis of the base glasses and glasses containing corroded waste revealed the
239 presence of diffuse scattering between $20^\circ < 2\theta < 40^\circ$ for the borosilicate compositions, MBS and MBS-
240 C (Figs. 2a and b). When analysed by SEM-EDX (Supplementary Fig. 1), the MBS and MAS base glass
241 compositions were homogeneous with no apparent phase separation. The MBS-C composition
242 exhibited striations of differing chemical composition (Figs. 3a and b) with the light regions enriched in
243 Al and U, whereas these elements were depleted in the regions of dark contrast (Fig. 3b). The presence
244 of such striations indicate that the synthesis method successfully promoted the desired heterogeneity
245 that may result from insufficient mixing of the dense uranium within a full scale process. For the
246 aluminosilicate compositions, MAS and MAS-C, two regions of diffuse scattering were apparent
247 between $15^\circ < 2\theta < 45^\circ$ which was interpreted as characteristic of the presence of two separated
248 amorphous phases, consistent with SEM observations of the microstructure shown below. Crystalline
249 inclusions were not present in either the base glasses nor the glasses immobilising the corroded waste,
250 in agreement with the absence of sharp Bragg reflections in the XRD data (Fig. 2b).

251

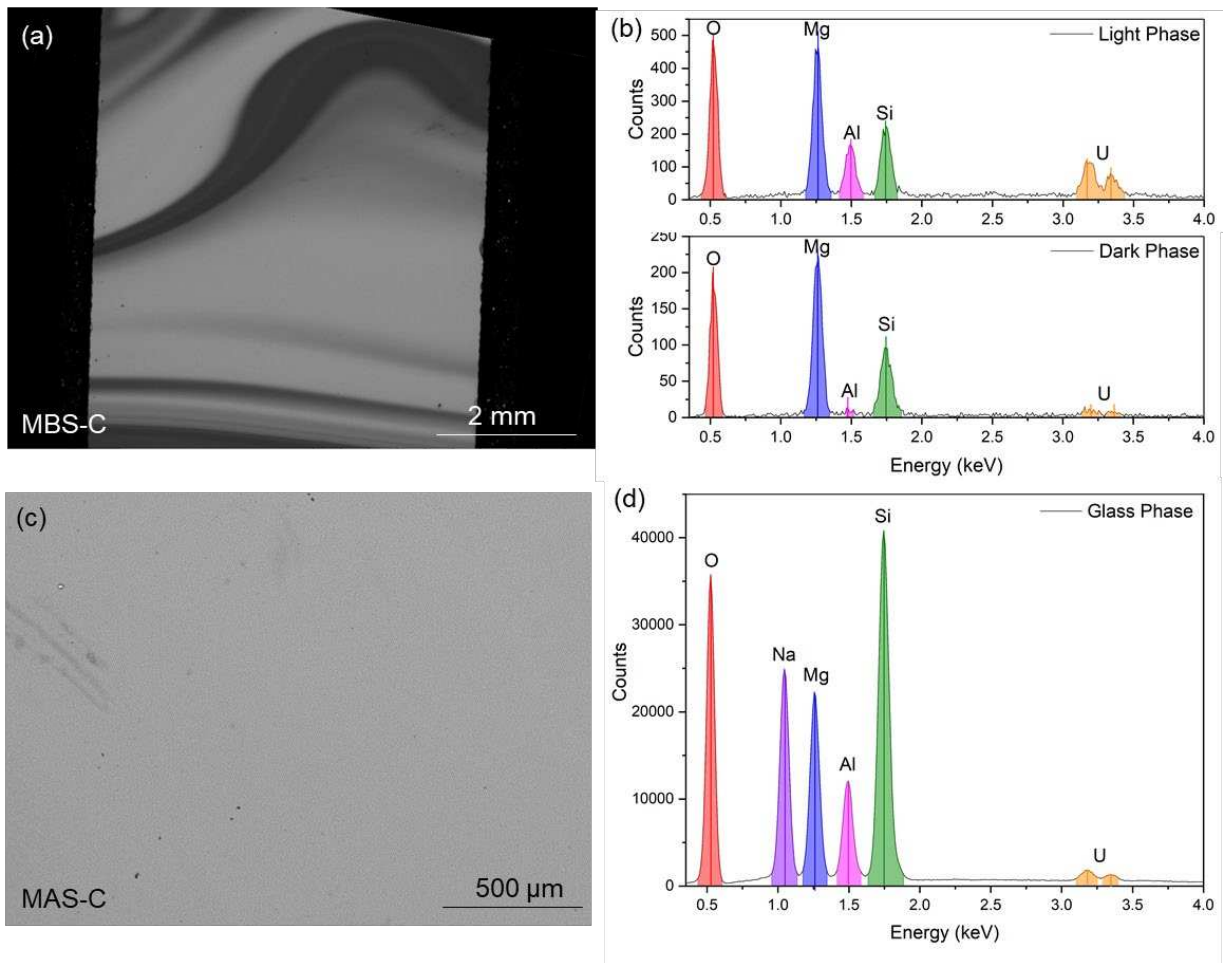


252

253 Fig. 2. X-ray diffraction patterns of (a) MBS and MAS base glasses; (b) MBS-C and MAS-C (corroded waste) glasses

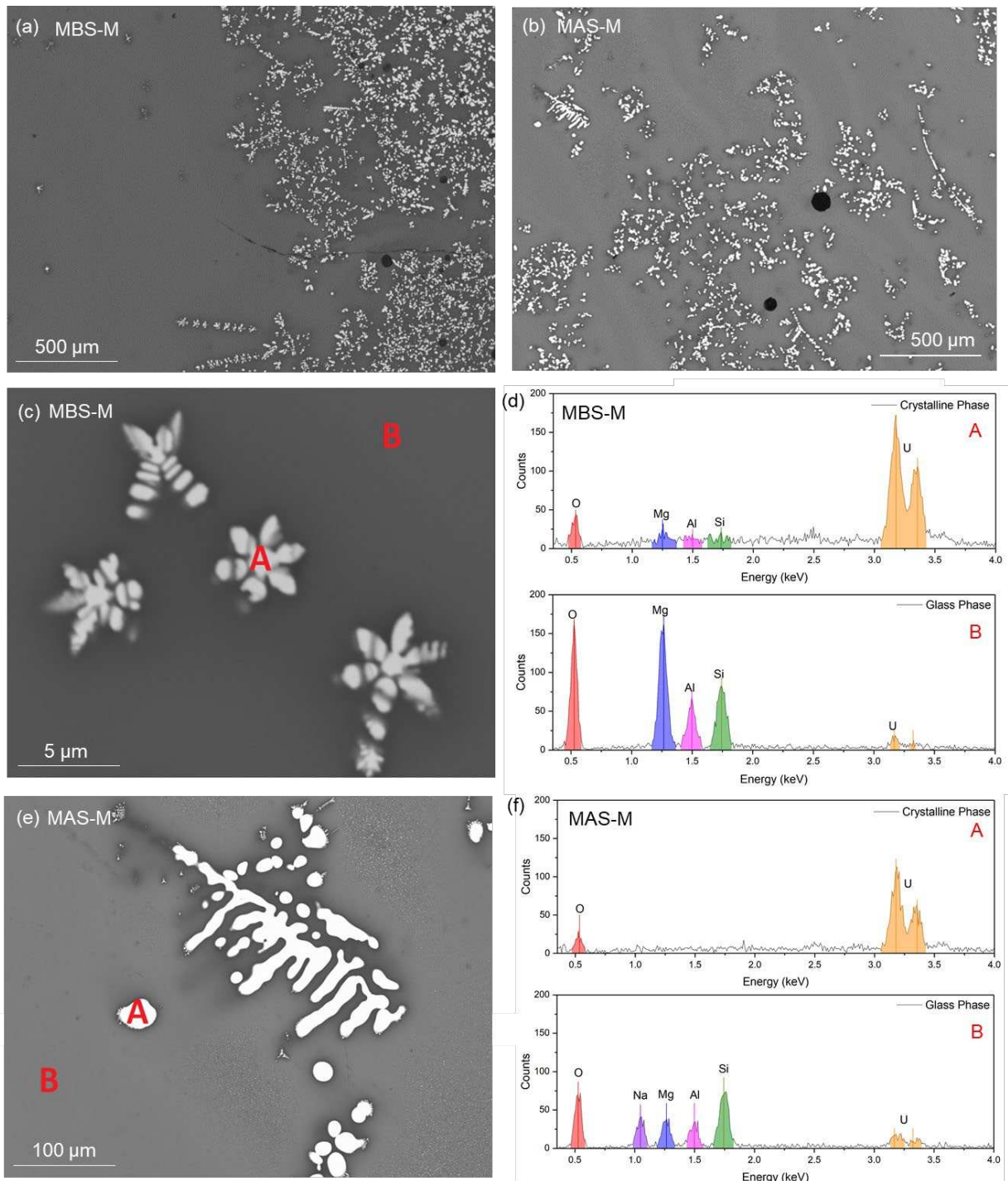
254 and; (c) MBS-M and MAS-M (metallic waste) glasses.

255



256
 257 **Fig. 3.** Back scattered electron image and EDX spectra of (a) MBS-C and; (b) MAS-C.
 258

259 In contrast to the base and corroded-waste glasses, the metallic waste-containing samples (MBS-M and
 260 MAS-M) exhibited sharp Bragg reflections confirming the presence of crystalline phases in addition to
 261 diffuse scattering (Fig. 2c). The XRD pattern of the borosilicate MBS-M glass confirmed the presence of
 262 crystalline UO_2 and U_3O_8 phases, whilst only UO_2 was apparent in the aluminosilicate MAS-M glass.
 263 Stratification of the MBS-M melt into a glass and a heavier slag, which settled on the bottom of the
 264 crucible (Fig. 1), means that the glassy portion was present as a thin layer, which may have encouraged
 265 oxidation and the formation of both UO_2 and U_3O_8 . SEM images confirmed the presence of dendritic
 266 and fused uranium-containing crystallites within the glass matrices of both samples (Fig. 4); dendritic
 267 crystallites (approximately 1.5 μm in diameter) formed predominantly in MBS-M (Figs. 4c and d), whilst
 268 fused crystals formed larger structures (approximately 3.5 μm in diameter) in MAS-M (Figs. 4e and f).
 269 Voids and air bubbles were also observed in the metallic waste glasses, likely due to the higher viscosity
 270 of the melts which trapped air bubbles. EDX spectra of the crystalline phases confirmed the presence
 271 of U and O, with other elements present due to over-sampling of the glass matrix by the electron beam.
 272



273

274

275

276

277

278 *3.3 Uranium incorporation*

279

280

281

Fig. 4. BSE-SEM-EDX data acquired for metallic waste-loaded glass compositions. Showing distribution of U-bearing crystallites in (a) MBS-M; and (b) MAS-M; (c) the dendritic morphology of U-crystallites in MBS-M and; (d) associated EDX spectra; (e) fused morphology of U-crystallites in MAS-M and; (f) associated EDX spectra.

The valence state of uranium in the glass matrix was evaluated in each of the four waste loaded glasses by μ -XANES analysis. Figure 5a displays the background subtracted and normalised U L₃ XANES data from the MAS and MBS waste loaded glasses compared with data from reference compounds with a

282 range of valence states: U^{4+} (UO_2), U^{5+} ($U_{0.5}Y_{0.5}Ti_2O_6$), and U^{6+} ($CaUO_4$). Figure 5b shows the first
283 derivative of the XANES data. Core-hole lifetime broadening of U L_3 -edge XANES data makes a definitive
284 assessment of the relative contributions of U^{4+} , U^{5+} and U^{6+} to the average valence difficult and
285 compositions with a mean valence state in excess of 5.0 will likely have some contribution from U^{6+} ,
286 which is typically incorporated in silicate glasses as the uranyl species $(UO_2)^{2+}$ [26, 27]. This species has
287 a diagnostic post-edge resonance at approximately 15 eV above the L_3 absorption edge (E_0) of uranium,
288 which arises from scattering by the uranyl O=U=O oxygen atoms [28, 29]. This is highlighted in Figures
289 5a and b by the dashed lines, exemplified by the uranyl-containing $CaU^{6+}O_4$ standard. Observation of
290 this post-edge resonance region indicates that all of the glass samples analysed contained a
291 contribution from $(UO_2)^{2+}$, indicating the effective oxidation of the metallic uranium feed in the thermal
292 treatment process. As noted by Prieur et al, the E_0 determined from the first derivative of the U L_3
293 XANES is not significantly different for UO_2^{2+} species in aqueous solution or in AUO_4 uranates ($A = Ca,$
294 Sr, Ba, Pb) [30].

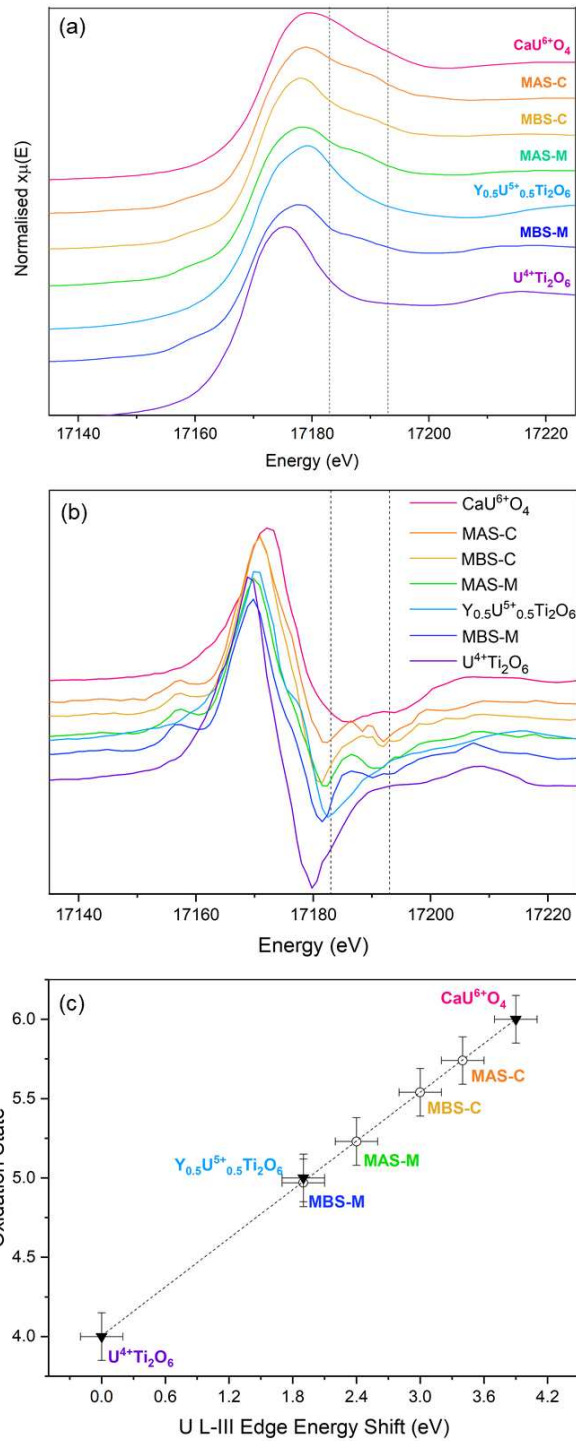
295

296 Furthermore, following correction to the absolute energy scale, using the known E_0 of Zr foil measured
297 simultaneously, the precise energy of the absorption edge was obtained (Table 3, Fig. 5c). Because this
298 energy is directly correlated to the valence state, a calibration line, based on the reference compounds
299 of known valence and coordination environment, can be utilised to extract the mean uranium valence
300 (Fig. 5c) [31]. For the MBS-M and MAS-M metallic waste formulations, this was found to be 4.9 ± 0.1
301 and 5.2 ± 0.1 , respectively. The mean valence of uranium dissolved in the glass of the corroded waste
302 form counterparts was higher, at 5.5 ± 0.1 and 5.7 ± 0.1 for MBS-C and MAS-C, respectively, reflecting
303 the more oxidised nature of the waste simulant. Uranium demonstrated a somewhat higher mean
304 valence in the MAS than the MBS glass fractions, likely a result of the higher processing temperature
305 used ($1500\text{ }^\circ\text{C}$ for MAS compared to $1250\text{ }^\circ\text{C}$ for MBS).

306

307

308



309

310

Fig. 5. X-ray Absorption Near Edge Spectroscopy data for the glass component of the waste forms and standard

311

compounds, taken at the U L₃-edge. Showing (a) U L₃-edge XANES region, highlighting the uranyl (UO_2)²⁺ region,

312

which exists between the dashed lines; (b) the first derivative of the U L₃-edge XANES region, highlighting the

313

uranyl region; and (c) the mean oxidation state of uranium in the glass phase of all compositions (open symbols)

314

and standards (closed symbols) versus E_0 energy shift. Error bars represent the error on the linear regression of

315

edge position of samples to the edge position of known standards.

316

317 **Table 3.** Extracted E_0 values and corresponding mean oxidation state of uranium, within the glass phase of the
 318 waste form materials and standard compounds, derived from U L_3 -edge XANES analysis.

Sample / Standard	E_0 (eV)	Oxidation State (± 0.1)
UTi ₂ O ₆	17166.4	4.0
MBS-M	17168.3	5.0
Y _{0.5} U _{0.5} Ti ₂ O ₆	17168.3	5.0
MAS-M	17168.8	5.2
MBS-C	17169.4	5.5
MAS-C	17169.8	5.7
CaUO ₄	17170.3	6.0

319

320

321 *3.4 Aqueous durability*

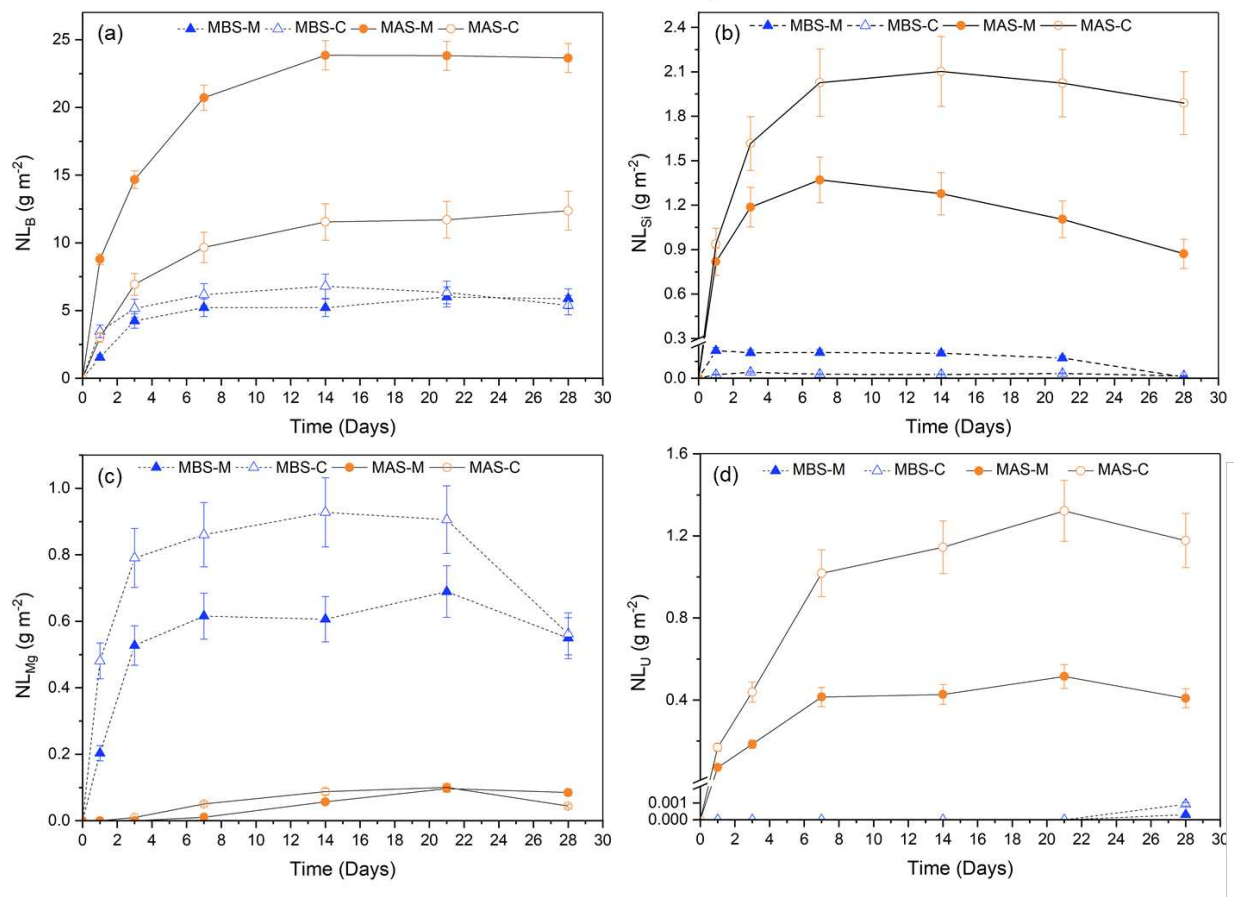
322 The normalised mass loss (NL_i) of B, Si, Mg and U were calculated for the corroded and metallic waste-
 323 loaded glass compositions (Fig. 6). Steady-state, residual rate (Stage II) dissolution [32, 33] was
 324 observed for all glass compositions after 14 days based on NL_B . After 28 days, for the corroded waste
 325 glasses, the NL_B of the aluminosilicate (MAS-C) was a factor of two greater than the borosilicate (MBS-
 326 C) counterpart. This is likely due to the pH of the two systems: the average pH(RT) was 12.1 ± 0.3 for
 327 MAS-C, while that of MBS-C sample was 8.4 ± 0.2 (Supplementary Fig. 2). These higher pH values in the
 328 MAS glass arise from the presence of Na in the formulation (which is absent from MBS); at high pH,
 329 silica is more soluble and, therefore, dissolution rates are expected to be higher than at lower pH values.
 330 Similarly, the NL_B of the MAS-M composition was a factor of five greater than the MBS-M counterpart,
 331 with pH values after 28 days of $pH 11.6 \pm 0.1$ and 8.6 ± 0.1 , respectively. Although the NL_B of MBS-M
 332 and MBS-C were similar, for the MAS compositions, there was a factor of 2.5 difference, with MAS-M
 333 giving the highest NL_B values. This is likely due to subtle differences in the composition of the MAS
 334 glasses (Table 2), in particular the content of boron, which was added as a tracer.

335

336 All compositions showed a decrease in NL_{Si} and NL_{Mg} between 21-28 days (Figs. 6b and c), whilst NL_B
 337 remained effectively constant; this behaviour, observed in other Mg-rich glasses, is indicative of the
 338 precipitation of magnesium (alumino)silicate secondary phases [34 – 36]. Despite the fact that the MAS
 339 compositions generally showed higher NL values than the MBS counterparts, the NL_{Mg} was almost a
 340 factor of 10 greater for MBS than MAS. This is likely due to pH effects, with the precipitation of $Mg(OH)_2$
 341 likely to occur at pH values of $>pH 10$, i.e., only in the MAS compositions.

342

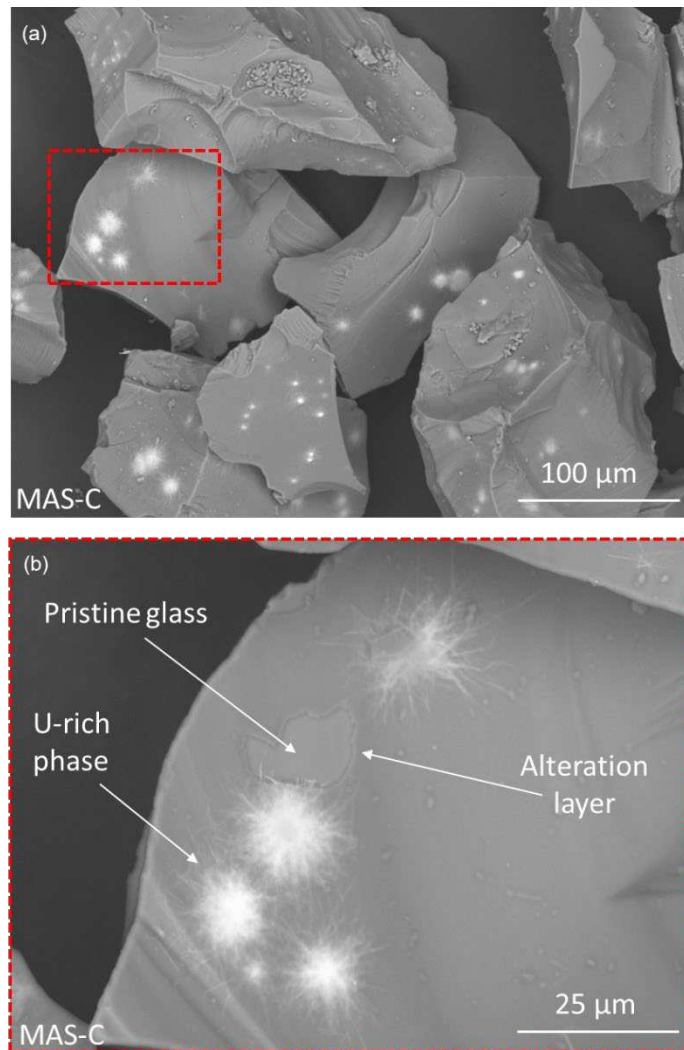
343 Over the duration of the experiments, significantly more U was released into solution from the MAS
 344 than the MBS compositions, and the release from the glasses loaded with corroded waste was always
 345 higher than the metallic counterparts (Fig. 6d). This is likely due to the lower oxidation state of uranium
 346 in the metallic waste-loaded glasses, since uranium oxidation states closer to +6 have a higher aqueous
 347 solubility than those close to 5+.
 348



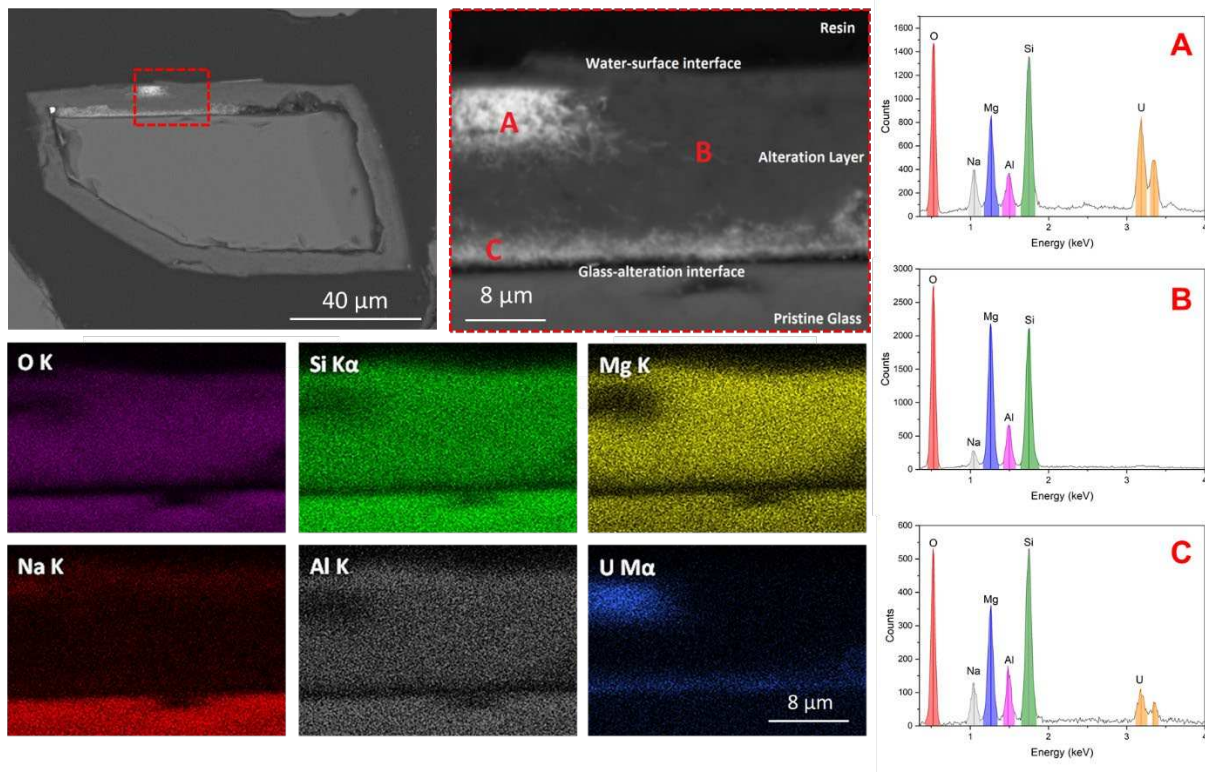
349 **Fig. 6.** Normalised mass loss of (a) B; (b) Si; (c) Mg and; (d) U (g m^{-2}) over a 28-day period, as determined using the
 350 PCT-B dissolution protocol, conducted at 90 °C, in UHQ and with $\text{SA/V} = 1200 \text{ m}^{-1}$. Error bars are the standard
 351 deviation of the sum of uncorrelated random errors of duplicate experiments.
 352

353
 354 BSE-SEM images of MAS-C particles altered for 28 days were observed to have formed spore-like U-rich
 355 secondary phases at the surface (Fig. 7) and were surrounded by an alteration layer, comprising a silica
 356 gel, rich in Al and Mg, and secondary precipitates. The entire alteration layer was approximately 10 μm
 357 thick in total (Fig. 8), noting that thickness measurements are an approximation due to uncertainty in
 358 particle orientation in cross-sectioned samples. It is interesting to note that Mg is present within the
 359 silica gel layer, since it typically tends to form secondary crystalline Mg-(alumino)silicate phases [34 –
 360 36]. However, in the absence of any other charge balancing species (e.g. Na^+ , Ca^{2+}) for $[\text{AlO}_4]^-$ and, at
 361 high pH, $\text{Si}(\text{OH})_3^-$ and $\text{Si}(\text{OH})_2^{2-}$, Mg^{2+} could play this role [34]. Bright regions of contrast observed in the

362 cross-sectioned BSE image of MAS-C (Region 'A' of Fig. 8) were rich in U, suggesting that the U-rich
363 spore like features had precipitated *within* the silica gel layer. Uranium was also concentrated at the
364 surface of the corroding glass (i.e. between the silica gel layer and the glass surface). There was an
365 enrichment of Na on the outer surface. The MAS-M composition exhibited a silica gel layer, 4 – 8 μm
366 thick, that was U-rich; spore-like U phases were either not observed or not resolved (Supplementary
367 Fig. 3).
368



369
370 **Fig. 7.** BSE-SEM images of MAS-C particles after 28 days of dissolution. U-rich secondary phases and an
371 alteration/gel layer were observed on top of the pristine glass.
372
373



374

375 **Fig. 8.** BSE-SEM cross-sectional images and associated EDX maps and spectra of MAS-C surrounded by an
 376 alteration layer formed after 28 days of dissolution at 90 °C in UHQ water.

377

378 In agreement with the lower NL_i values when compared to the aluminosilicate compositions, the
 379 alteration layer formed on the borosilicate MBS-C sample was less extensive (Supplementary Fig. 4), at
 380 $\sim 1 \mu\text{m}$ thick. This thickness is not sufficient to confer confident elemental analysis by EDX at the
 381 resolution employed, however, the composition of the layer was tentatively identified to contain Al,
 382 Mg and Si (Supplementary Fig. 5). An alteration layer was not observed on MBS-M
 383 (Supplementary Fig. 4).

384

385 Geochemical modelling of the solution leachate after 28 days indicated that numerous secondary
 386 crystalline phases were thermodynamically favourable to form under the test conditions
 387 (Supplementary Table 1), including the Mg-rich clay minerals talc $[\text{Mg}_3\text{Si}_4\text{O}_{10}(\text{OH})_2]$, saponite-Mg
 388 $[\text{Mg}_{3.165}\text{Al}_{0.333}\text{Si}_{3.67}\text{O}_{10}(\text{OH})_2]$ [35, 37], sepiolite $[\text{Mg}_4\text{Si}_6\text{O}_{15}(\text{OH})_2 \cdot 6\text{H}_2\text{O}]$ [38] and chrysotile
 389 $[\text{Mg}_3\text{Si}_2\text{O}_5(\text{OH})_4]$, as well as the Mg-hydroxide, brucite $[\text{Mg}(\text{OH})_2]$. The uranyl silicate mineral, soddyite
 390 $(\text{UO}_2)_2(\text{SiO}_4) \cdot 2\text{H}_2\text{O}$, was predicted to be saturated in solution, however, the precipitated U-phases
 391 observed by EDX did not contain Si. Hydrated uranium oxide phases, $\text{UO}_3 \cdot 0.9\text{H}_2\text{O}$ and $\text{UO}_3 \cdot 2\text{H}_2\text{O}$ were
 392 predicted to be in equilibrium with the solution, suggesting they may be thermodynamically favourable
 393 to form. XRD analysis of the glasses after dissolution was unable to identify any additional phases to
 394 those already present within the glass (Supplementary Fig. 6). However, it was possible to observe a

395 shift in the lattice position of the UO_2 peaks in the MAS-M XRD pattern, consistent with partial oxidation
396 to UO_{2+x} . Both of the corroded waste-loaded glass samples remained x-ray amorphous after 28 day PCT-
397 B tests with no significant crystalline Bragg reflections detected, however, two minor peaks were
398 identified (Supplementary Fig. 6), which could be loosely indexed to the major reflections of sepiolite
399 $[\text{Mg}_4\text{Si}_6\text{O}_{15}(\text{OH})_2 \cdot 6\text{H}_2\text{O}]$, in agreement with the geochemical modelling.

400

401 The bulk dissolution methods applied in this study to heterogeneous wastefoms cannot discriminate
402 the contribution of different components, and the dissolution behaviour may be dominated by one or
403 more less durable components. Nevertheless, it is the overall material response, assessed using a
404 standardised method, that is of interest in an early assessment of potential disposability. To fully
405 understand the contribution of the component phases to the overall dissolution behaviour, spatially
406 resolved investigations of surface retreat rates by atomic force microscopy and vertical scanning
407 interferometry are planned.

408

409 *3.5 Efficacy of MAS and MBS glasses for Magnox Sludge immobilisation*

410 The presence of B_2O_3 in concentrations of >20 mol. % allowed melting of the borosilicate glass
411 compositions at lower temperatures than the aluminosilicate counterparts. Lower melt temperatures
412 are preferable for radioactive waste glasses due to compatibility with industrial vitrification plants,
413 which typically operate below 1200 °C and also because lower melt temperatures reduce the volatility
414 of radionuclides such as Cs [39], which will be present at low concentrations as a fission product in
415 degraded fuel residues. For these reasons, aluminosilicate glass compositions are considered to be less
416 promising for the immobilisation of Magnox sludge wastes, within the constraints of this study.

417

418 Samples produced from the corroded waste stream were generally visually homogenous (with
419 exception of U-poor striations), whereas samples immobilising the metallic waste stream partitioned
420 into a glass and a glassy slag-like fraction. The partial crystallisation of glasses produced from the
421 metallic waste simulant does not pose a fundamental barrier to vitrification of Magnox sludge wastes
422 in these glass composition; a definitive assessment would require a pilot scale demonstration
423 experiment, e.g. using Joule heated batch melter technology, where realistic melt convection would
424 provide an understanding of the distribution and fraction of crystalline components, potentially
425 negating the partitioning observed in this bench-scale study. If necessary, the waste loading could be
426 reduced to achieve an acceptable crystalline component. Current UK waste vitrification involves
427 melting calcined waste with a glass frit in an induction heated melter. However, as the Mg content in

428 these vitrified wasteforms is derived from the waste stream, a Joule heated ceramic melter system,
429 where the glass formers could be batched as additives, may be more appropriate.

430

431 XANES analysis demonstrated that both the metallic and corroded waste streams were oxidised in the
432 glass melt without mechanical stirring or bubbling. Such behaviour simplifies the production of glass at
433 larger scales and reduces the amount of secondary waste produced; however, phase segregation in the
434 melts containing the metallic waste stream and phase separation in the corroded waste MBS-C
435 composition suggests that stirring or bubbling could be beneficial. Due to the increased melting
436 temperature and melt duration, U in the aluminosilicate samples was more oxidised than in the
437 equivalent borosilicate samples as higher temperatures provided more oxidising conditions. Glasses
438 immobilising the corroded waste were found to have higher U oxidation states than their metallic
439 counterparts, due to the initial batch components: the corroded waste stream contained oxidised
440 uranium (U_3O_8) and only small amounts of metal, whereas the metallic waste stream glasses were
441 batched with larger quantities of metallic U. The oxidation state of uranium is important since it
442 influences its mobility in aqueous environments, and glass compositions with U in 4+ oxidation states
443 would be preferential for disposal [35, new 40]. The glass compositions with higher mean uranium
444 oxidation states demonstrated the greatest U normalised mass loss, indicating that the addition of
445 metallic uranium to the glass may be beneficial for the durability, at least in the short-term.

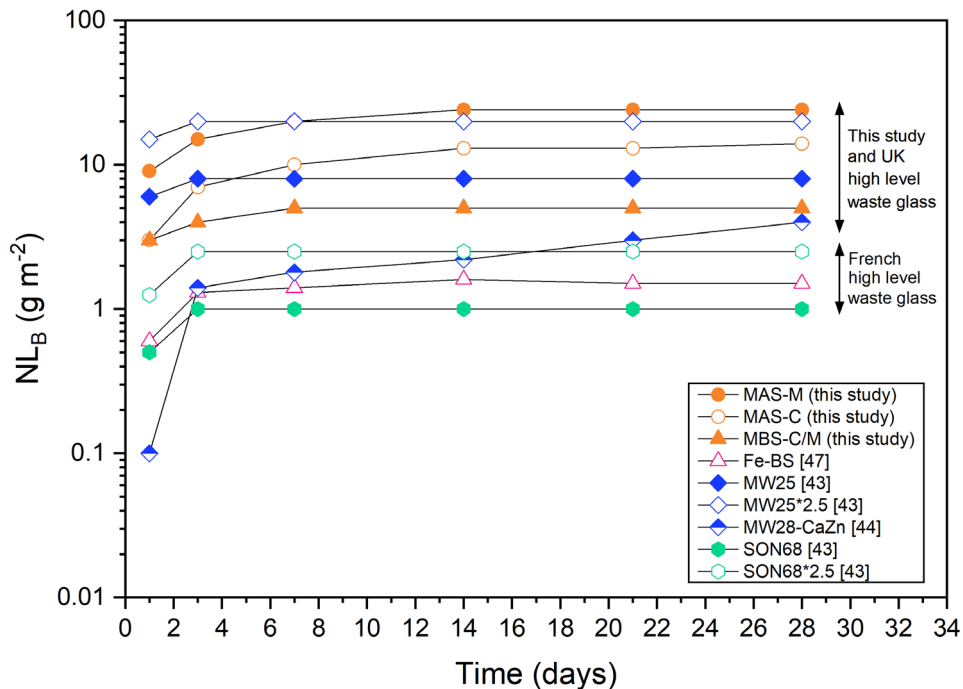
446

447 Figure 9 compares the normalised mass loss of B of each of the vitrified Magnox sludge compositions
448 investigated in the present study work with that other radioactive waste glass simulants, including high
449 level waste glass compositions. Boron is here used since it is a reliable tracer for glass dissolution as it
450 does not usually become incorporated within glass alteration layers. The test conditions of all glasses
451 in this figure are comparable, and where a particular composition is denoted as “*2.5”, this indicates
452 that a surface area conversion factor has been applied to convert the SA measured by BET to the
453 geometric surface area (assuming spherical geometry) [41]. It can be observed that the Magnox sludge
454 glass compositions have NL_B values that are of the same order of magnitude as the UK simulant high
455 level waste glass compositions, MW25 and CaZnMW28 [42 – 46] and one order of magnitude higher
456 than the French high level waste simulant, SON68 [43]. The MBS compositions have a durability
457 between those of the UK and French compositions (Fig. 9).

458

459 In comparison with an Fe-alkali borosilicate glass also developed for Magnox sludge immobilisation [47],
460 which comprised a more complex waste formulation, used a lower average waste composition (30
461 wt. % as opposed to the bounding extreme wastes used in this study (31.7 – 56.3 wt.%), and Ce as a

462 surrogate for U, the chemical durability of the glasses developed in the present study was lower. This
 463 is likely due to the incorporation of significantly higher concentrations of MgO in the present study,
 464 ranging from 17.0 to 41.6 wt.%, compared with only 22.15 wt.% in Tan et al [47]. Also, the addition of
 465 Ce as a U surrogate cannot replicate the chemical behaviour during dissolution; oxidised Ce^{4+} is more
 466 insoluble than reduced Ce^{3+} . Nevertheless, it can be stated that the inherent durability of the MAS glass
 467 (based on the normalised mass loss of boron), and in particular the MBS glasses, is comparable to that
 468 of high level waste glass compositions. Such material is already destined for disposal within a geological
 469 facility, but possesses a significantly higher radiation hazard; therefore, the glasses developed in the
 470 current study, which are of lower hazard and equal durability, appear to be suitable candidates for the
 471 immobilisation of Magnox sludge, from a chemical durability perspective.
 472



473
 474 **Fig. 9.** The normalised mass loss of boron from the Magnox sludge glasses developed in the current study,
 475 compared with those from other simulant radioactive waste glass compositions. All data were acquired by the
 476 same PCT-B test protocol (at 90 °C in UHQ water with $SA/V = 1200 \text{ m}^{-1}$). Glasses denoted with “*2.5” have had a
 477 surface area correction applied to convert the SA measured by BET to the geometric surface area (assuming
 478 spherical geometry) [41].

479
 480 Given that the MBS glass compositions possessed favourable thermal and durability characteristics,
 481 their application in the immobilisation of Magnox sludge is considered. Firstly, if the 2,398 m³ of Magnox
 482 sludge residing in the FGMSP and SIXEP bulk storage tanks were to be vitrified, a net reduction in the
 483 volume of waste to be disposed of 60% could be achieved, in comparison with the current baseline plan

484 of cementation in 500 L drums [17]. Secondly, should the MSSS decommissioning and waste processing
485 scheme allow for extraction of Magnox sludge, together with the other components (Magnox swarf,
486 Al/Al(OH)₃, U/UO₂/U₃O₈, miscellaneous β/γ waste (some of which may not be suitable for vitrification,
487 e.g. sealed cans and aggregate) residing within the MSSS, and vitrification were to be achieved through
488 application of an in-can melter technology, there is potential for a volume reduction of 96% compared
489 with the baseline treatment strategy of cementation in almost 12,000 3m³ boxes. Since the cost of
490 disposal for intermediate level waste in a GDF is estimated, at the time of writing, as £8,990 per m³ [48],
491 the financial saving from disposing vitrified Magnox sludge waste from these locations at the Sellafield
492 site, notwithstanding the costs of vitrification plant construction and operation, can be estimated as
493 approximately £25 million for FGMSP, and £300 million for MSSS.

494

495 4. Conclusion

496 In this study magnesium aluminosilicate and magnesium borosilicate glass systems were produced that
497 passively oxidised and incorporated metallic uranium and magnesium representative of Magnox sludge
498 wastes present in the First Generation Magnox Storage Ponds at Sellafield in the UK. Two bounding
499 extremes of the waste – a metallic form and corroded form - encompassing the whole anticipated
500 waste envelope were largely incorporated into a stable vitrified product. Magnesium borosilicate
501 compositions melted below 1250 °C which is compatible with the glass melter technology currently
502 under consideration for thermal treatment of decommissioning wastes. Furthermore, borosilicate
503 glasses possessed greater chemically durable than their aluminosilicate counterparts and all glass
504 compositions demonstrated durability that is comparable to UK and French high level waste glass
505 compositions.

506 Declaration of Competing Interest

507 The authors declare that they have no known competing financial interests or personal relationships
508 that could have appeared to influence the work reported in this paper.

509 Acknowledgements

510

511 We acknowledge financial support from the Nuclear Decommissioning Authority (NDA) and EPSRC
512 under grant numbers EP/G037140/1, EP/S01019X/1 and EP/N017374/1. This project has received
513 funding from the Euratom research and training programme 2014-2018 under grant agreement No
514 755480 (THERAMIN) and was supported by the IAEA CRP on Management of Severely Degraded Spent
515 Fuel and Corium. This research utilised the HADES/MIDAS facility at the University of Sheffield
516 established with financial support from EPSRC and BEIS, under grant EP/T011424/1 [49] and the Henry

517 Royce Institute for Advanced Materials, funded through EPSRC grants EP/R00661X/1, EP/S019367/1,
518 EP/P02470X/1 and EP/P025285/1, for ICP access at Royce@Sheffield. We acknowledge the Paul
519 Scherrer Institut, Villigen, Switzerland for provision of synchrotron radiation beamtime at beamline X05
520 of the SLS and would like to thank Daniel Grolimund for his assistance.
521

522 References

- 523 [1] S. Morgan, M. Barnes, G. Randall, Progress towards treating the sludges produced during spent fuel
524 processing, Proceedings of the Waste Management Conference, WM2019, March 3 – 7, Phoenix,
525 Arizona (2019)
- 526 [2] J. Cronin, N. Collier, Corrosion and expansion of grouted Magnox. *Miner. Mag.* 76 (2012) 2901–2909.
- 527 [3] J. S. Clarke, Conditioning of legacy radioactive wastes requiring additional treatment, Ph.D Thesis,
528 The University of Sheffield (2018)
- 529 [4] A. Hoch, M. Wilkes, Modelling the Expansion and Cracking of Grouted Wasteforms Containing Mild
530 Steel or Magnox, AMEC/002053/001 Issue 2 (2016)
- 531 [5] A. Covill, N.C. Hyatt, J. Hill, N.C. Collier, Development of magnesium phosphate cements for
532 encapsulation of radioactive waste. *Adv. Appl. Ceram.* 6753 (2011) 151–156.
- 533 [6] L.J. Gardner, C.L. Corkhill, S.A. Walling, J.E. Vigor, C.A. Murray, C.C. Tang, J.L. Provis, N.C. Hyatt, Early
534 age hydration and application of blended magnesium potassium phosphate cements for reduced
535 corrosion of reactive metals. *Cem. Concr. Res. Manuscript accepted (in press)*
- 536 [7] N.C. Hyatt, M. James, Thermal treatment of ILW. *Nucl. Eng. Int.* (2013)
537 <https://www.neimagazine.com/features/featurethermal-treatment-of-ilw/>
- 538 [8] N.C. Hyatt, R.R. Schwarz, P.A. Bingham, M.C. Stennett, C.L. Corkhill, P.G. Heath, R.J. Hand, M. James,
539 A. Pearson, S. Morgan, Thermal treatment of simulant plutonium contaminated materials from the
540 Sellafield site by vitrification in a blast-furnace slag. *J. Nuc. Mater.* 444 (2014) 186-199.
- 541 [9] L. Boast, M.C. Stennett, N.C. Hyatt, Thermal treatment of plutonium contaminated material (PCM)
542 waste. *MRS Adv.* 2 (2017) 735 – 740.
- 543 [10] S.A. Walling, M.N. Kauffmann, L.J. Gardner, D.J. Bailey, M.C. Stennett, C.L. Corkhill, N.C. Hyatt,
544 Characterisation and disposability assessment of multi-waste stream in-container vitrified products
545 for higher activity radioactive wastes. *J. Haz. Mater.* 401 (2021) 123764.
- 546 [11] A. Goel, J.S. McCloy, R. Pokorny, A.A. Kruger, Challenges with vitrification of Hanford High-Level
547 Waste (HLW) to borosilicate glass – An overview. *J. Non-Cryst. Solids: X.* 4 (2019) 100033.
- 548 [12] D.J. Backhouse, C.L. Corkhill, N.C. Hyatt, R.J. Hand. Investigation of the role of Mg and Ca in the
549 structure and durability of aluminoborosilicate glass. *J. Non-Cryst. Solids.* 512 (2019) 41.

- 550 [13] M. Kim, C.L. Corkhill, N.C. Hyatt, J. Heo. Development, characterisation and dissolution behaviour
551 of calcium-aluminoborate glass wastefoms to immobilise rare-earth oxides. *Scientific Reports*. 8
552 (2018) 5320.
- 553 [14] H. Zhang, C.L. Corkhill, P.G. Heath, R.J. Hand, M.C. Stennett, N.C. Hyatt. Effect of Zn- and Ca-oxides
554 on the structure and durability of simulant alkali borosilicate glasses for immobilisation of UK high
555 level wastes. *J. Nucl. Mater.* 462 (2015) 321.
- 556 [15] E.M. Levin, C.R. Robbins, H.F. McMurdie, *Phase Diagrams For Ceramists: Volume 1*. Columbus,
557 Ohio: The American Ceramic Society INC. (1964)
- 558 [16] E.M. Levin, C.R. Robbins, H.F. McMurdie, *Phase Diagrams For Ceramists: Volume 2 - 1969*
559 *Supplement*. Columbus, Ohio: The American Ceramic Society INC. (1969)
- 560 [17] Nuclear Decommissioning Authority, UK Radioactive Waste Inventory (accessed October 2020)
561 <https://ukinventory.nda.gov.uk/>
- 562 [18] B.E. Scheetz, W.P. Freeborn, D.K. Smith, C. Anderson, M. Zolensky, W.B. White, The role of boron
563 in monitoring the leaching of borosilicate glass waste forms. *Mater. Res. Soc. Proc.* 44 (1984) 129,
564 doi.org/10.1557/PROC-44-129
- 565 [19] C.N. Borca, D. Grolimund, M. Willimann, B. Meyer, K. Jefimos, J. Vila-Comamala, C. David, The
566 microXAS beamline at the swiss light source: Towards nano-scale imaging. *J. Phys. Conf. Ser.* 186
567 (2009) 012003.
- 568 [20] D.E. Crean, F.R. Livens, M.C. Stennett, D. Grolimund, C.N. Borca, N.C. Hyatt, Micro-analytical X-ray
569 imaging of depleted uranium speciation in environmentally aged munitions residues. *Env. Sci.*
570 *Technol.* 48 (2014) 1467 – 1474.
- 571 [21] H. Ding, M.C. Dixon Wilkins, C. Gausse, L.M. Mottram, S. Sun, M.C. Stennett, D. Grolimund, R.
572 Tappero, S. Nicholas, N.C. Hyatt, C.L. Corkhill, Safely probing the chemistry of Chernobyl nuclear fuel
573 using micro-focus X-ray analysis. *J. Mater. Chem. A*. *Manuscript accepted, in press*.
- 574 [22] B. Ravel, M. Newville, Athena, Artemis, Hephaestus: data analysis for X-ray absorption
575 spectroscopy using IFEFFIT. *J. Synch. Rad.* 12 (2005) 537 – 541.
- 576 [23] S.T. Barlow, D.J. Bailey, A.J. Fisher, M.C. Stennett, C. Gausse, H. Ding, V.A. Krasnov, S.Y. Sayenko,
577 N.C. Hyatt, C.L. Corkhill, Synthesis, characterisation and corrosion behaviour of simulant Chernobyl
578 nuclear meltdown materials. *Npj Mater. Deg.* 4 (2020) 3.
- 579 [24] C.L. Corkhill, D.E. Crean, D.J. Bailey, C. Makepeace, M.C., Stennett, R. Tappero, D. Grolimund, N.C.
580 Hyatt, Multi-scale investigation of uranium attenuation by arsenic at an abandoned uranium mine,
581 South Terras. *Npj Mater. Deg.* 1 (2017) 19.

- 582 [25] ASTM International C1285-14, Standard Test Methods for Determining Chemical Durability of
583 Nuclear, Hazardous, and Mixed Waste Glasses and Multiphase Glass Ceramics: The Product
584 Consistency Test (PCT) (2014)
- 585 [26] A.J. Connelly, N.C. Hyatt, K.P. Travis, R.J. Hand, M.C. Stennett, A.S. Gandy, A.P. Brown, D.C.
586 Apperley, The effect of uranium oxide additions on the structure of alkali borosilicate glasses. *J. Non-*
587 *Cryst. Solids.* 378 (2013) 282 – 289.
- 588 [27] F. Farges, C.W. Ponader, G. Calas, G.E. Brown, Structural environments of incompatible elements
589 in silicate glass/melt systems: II. UIV, UV, and UVI. *Geochim. Cosmochim. Acta*, 56 (1992) 4205 –
590 4220.
- 591 [28] C. Den Auwer, E. Simoni, S. Conradson, C. Madic, Investigating Actinyl Oxo Cations by X-ray
592 Absorption Spectroscopy. *Eur. J. Inorg. Chem.* 21 (2003) 3843 – 3859.
- 593 [29] C. Fillaux, J-C. Berthet, S.D. Conradson, P. Guilbaud, D. Guillaumont, C. Hennig. P. Moisy, J. Rogues,
594 E. Simioni, D.K. Shuh, T. Tyliczszak, I. Castro-Rodriguez, C. Den Auwer, Combining theoretical
595 chemistry and XANES multi-edge experiments to probe actinide valence states. *Cr. Chim.*, 10 (2007)
596 859 – 871.
- 597 [30] D.B. Prieur, K. Popa, J.-F. Vigier, A.C. Schienost, P.M. Martin. Crystallographic structure and charge
598 distribution of AUO_4 and A_3O_6 uranates ($A = Ca, Sr, Ba$ or Pb). *J. Nucl. Mater.* 516 (2019) 303.
- 599 [31] B. Kosog, H.S. La Pierre, M.A. Denecke, F.W. Heinemann, K. Meyer, Oxidation State Delineation via
600 U L_{III} -Edge XANES in a Series of Isostructural Uranium Coordination Complexes. *Inorg. Chem.* 51
601 (2012) 7940 – 7944.
- 602 [32] P. Frugier, S. Gin, Y. Minet, T. Chave, B. Bonin, N. Godon, J-E. Lartigue, P. Jollivet, A. Ayrat, L. De
603 Windt, G. Santarini, SON68 nuclear glass dissolution kinetics: Current state of knowledge and basis
604 of the new GRAAL model. *J. Nucl. Mater.* 380 (2008) 8 – 21.
- 605 [33] J.D. Vienna, J.V. Ryan, S. Gin, Y. Inagaki, Current understanding and remaining challenges in
606 modelling long-term degradation of borosilicate nuclear waste glasses. *Int. J. Appl. Glass. Sci.* 4
607 (2013) 283 – 394.
- 608 [34] B. M. J. Thien, N. Godon, A. Ballestro, S. Gin, A. Ayrat, The dual effect of magnesium on the long-
609 term alteration rate of AVM nuclear waste glasses. *J. Nucl. Mater.* 427 (2012) 297 – 310.
- 610 [35] B. Fleury, N. Godon, A. Ayrat, S. Gin, SON68 glass dissolution driven by magnesium silicate
611 precipitation. *J. Nucl. Mater.* 442 (2013) 17 – 28.
- 612 [36] H. Arena, D. Rebiscoul, R. Podor, E. Garces, M. Cabie, J-P. Mestre, N. Godon, Impact of Fe, Mg and
613 Ca on glass alteration: Interconnected processes. *Geochim. Cosmochim. Acta.* 239 (2018) 420 – 445.

614 [37] A.J. Fisher, M.N.B. Imran, C. Mann, C. Gausse, R.J. Hand, N.C. Hyatt, C.L. Corkhill, Short
615 communication: The dissolution of UK simulant vitrified high-level-waste in groundwater solutions.
616 J. Nucl. Mater. 538 (2020) 152245.

617 [38] C.L. Corkhill, N.J. Cassingham, P.G. Heath, N.C. Hyatt, Dissolution of UK High-Level Waste Glass
618 Under Simulated Hyperalkaline Conditions of a Co-located Geological Disposal Facility. Int. J. Appl.
619 Glass. Sci. 4 (2013) 341 – 356.

620 [39] J.D. Vienna, The Effects of Temperature and Composition on the Solubility of Chromium in Multi-
621 Component Alkali-Borosilicate Glass Melts. Ph.D Thesis, Washington State University (2002)

622 [40] C.M. Jantzen, C.L. Trivelpiece, Uranium dissolution and geochemical modelling in anoxic and oxic
623 solutions. MRS. Adv. 2 (2017) 705 – 710.

624 [41] M. Fournier, A. Ull, E. Nicoleau, Y. Inagaki, M. Odorico, P. Frugier, S. Gin, Glass dissolution rate
625 measurement and calculation revisited. J. Nucl. Mater. 476 (2016) 140 – 154.

626 [42] C. Brookes, M. Harrison, A. Riley, C.J. Steele, The effect of increased waste loading on the durability
627 of high level waste glass. Mat. Res. Soc. Symp. Proc. 1265 (2010) 109 – 114.

628 [43] E. Curti, J.L. Crovisier, G. Morvan, A.M. Karpoff, Long-term corrosion of two nuclear waste
629 reference glasses (MW and SON68): A kinetic and mineral alteration study. Appl. Geochem. 21
630 (2006) 1152 – 1168.

631 [44] A.J. Fisher, M.T. Harrison, N.C. Hyatt, R.J. Hand, C.L. Corkhill, The dissolution of simulant UK Ca/Zn-
632 modified nuclear waste glass: Insight into Stage III behaviour. MRS. Adv. 5 (2020) 103 – 109.

633 [45] M.T. Harrison, G.C. Brown, Chemical durability of UK vitrified high level waste in Si-saturated
634 solution. Mat. Let. 221, (2018) 154 – 156.

635 [46] T.L. Goût, M.T. Harrison, I. Farnan, Evaluating the temperature dependence of Magnox waste glass
636 dissolution. J. Non-Cryst. Solids. 518 (2019) 75 – 84.

637 [47] S. Tan, N. Kirk, M. Marshall, O. McGann, R.J. Hand, Vitrification of an intermediate level Magnox
638 sludge waste. J. Nucl. Mater. 515 (2019) 140 – 154.

639 [48] Department of Energy and Climate Change, 2011. Waste Transfer Pricing Methodology for the
640 disposal of higher activity waste from new nuclear power stations, [HM Government Department of
641 Energy and Climate Change Report](#).

642 [49] N.C. Hyatt, C.L. Corkhill, M.C. Stennett, R.J. Hand, L.J. Gardner, C.L. Thorpe, The HADES Facility for
643 High Activity Decommissioning Engineering and Science: Part of the UK National Nuclear User
644 Facility. IOP Conf. Ser-Mat Sci. 818 (2020) 012022.

645

646